Green synthesis of ultrapure $La(OH)_3$ nanoparticles by one-step method through spark ablation and electrospinning and its application to phosphate removal

Li, Shiyang; Huang, Xiangfeng; Wan, Zhengyu; Liu, Jia; Lu, Lijun; Peng, Kaiming; Schmidt-Ott, Andreas; Bhattarai, Rabin

DOI
10.1016/j.cej.2020.124373

Publication date
2020

Document Version
Accepted author manuscript

Published in
Chemical Engineering Journal

Citation (APA)
Li, S., Huang, X., Wan, Z., Liu, J., Lu, L., Peng, K., Schmidt-Ott, A., & Bhattarai, R. (2020). Green synthesis of ultrapure $La(OH)_3$ nanoparticles by one-step method through spark ablation and electrospinning and its application to phosphate removal. *Chemical Engineering Journal*, *388*, Article 124373. https://doi.org/10.1016/j.cej.2020.124373

Green synthesis of ultrapure $La(OH)_3$ nanoparticles by one-step method through spark ablation and electrospinning and its application to phosphate removal

Shiyang Li[a], *Xiangfeng Huang*[a*], *Zhengyu Wan*[b], *Jia Liu*[a], *Lijun Lu*[a], *Kaiming Peng*[a], *Andreas Schmidt-Ott*[c], *Rabin Bhattarai*[d]

[a] College of Environmental Science and Engineering, State Key Laboratory of Pollution Control and Resource Reuse, Ministry of Education Key Laboratory of Yangtze River Water Environment, Shanghai Institute of Pollution Control and Ecological Security, Tongji University, Shanghai 200092, People's Republic of China

[b] Phenom Scientific, 88 Keyuan Road, Shanghai 200092, People's Republic of China

[c] Faculty of Applied Science, Delft University of Technology, Julianalaan 136, 2628 BL Delft, The Netherlands

[d] Department of Agricultural and biological Engineering, University of Illinois at Urbana Champaign, 1304 W Pennsylvania Ave, Urbana IL 61801, USA

Corresponding author: Xiangfeng Huang, College of Environmental Science and Engineering, State Key Laboratory of Pollution Control and Resource Reuse, Ministry of Education Key Laboratory of Yangtze River Water Environment, Shanghai Institute of Pollution Control and Ecological Security, Tongji University, Shanghai

200092, People's Republic of China. Tel/Fax: +86 21 65982592. Email:

hxf@tongji.edu.cn.

Abstract

$La(OH)_3$ metal engineered nanoparticles (MENPs) are efficient phosphate binders; however, complex synthesis procedures and purity as well as agglomeration issues impede their development and practical applications. Herein, a green and a one-step method in combination with the spark ablation aerosol technology and electrospinning is proposed for the synthesis of $La(OH)_3$ MENPs; further, their application as phosphate binders are elucidated as a proof the concept. Material characterization results confirm the successful synthesis of ultrapure $La(OH)_3$ MENPs, which has not been achieved before via an environmentally friendly one-step procedure . Small angle X-ray scattering and X-ray photoelectron spectroscopy etching results show that $La(OH)_3$ MENPs loading on the electrospun nanofibers are uniform in both two and three dimensions. The comparative tests revealed a high phosphate adsorption capacity (110.8 mg P/g La) and indicted that the $La(OH)_3$ MENPs perform well; this was observed even under the interference of coexisting ions (Cl^-, SO_4^{2-}, NO_3^-, and F^-) at different pH values. After three cycles of solution-shaking treatment, the release of $La(OH)_3$ was less than 1 wt% (0.5 wt%), which was acceptable for an adsorbent. These results indicate that the $La(OH)_3$ MENP-loaded nanofibers are practical phosphate binders due to the simple production methods, low manufacturing cost, and impressive capacity. The proposed method significantly shortens the loading process and is a promising alternative for not only the synthesis of the adsorbent, but also for other engineering materials where loading is needed.

Keywords: $La(OH)_3$ nanoparticles, gas-phase coalescence, controllable particle sizes, industrialization potential, phosphorus removal, eutrophication

1. Introduction

Phosphorus is the key nutrient element to trigger eutrophication. However, the concentration of phosphorus in natural water is relatively low (0.1-0.5mg P/L), and it is difficult to remove phosphorus in the case of large flow and volume in rivers and lakes [1]. The use of metal engineered nanoparticles (MENPs) (especially with the rare earth element MENPs) as nano-finished adsorbent materials is one of the most effective ways to solve this problem [2, 3].

However, the development of practically functional MENPs is not easy. In the fields of filtration, adsorption, catalysis, energy conversion, storage, sensor technology and development of medicinal products, the size, purity, agglomeration, anchoring, cost, and recovery of MENPs are the practical considerations during design and application [4]. Multiple studies and application practices show that the "nano function" of the MENPs is distinct when the particles are small (diameters 50 nm or less), pure, uniform, and dispersed [5-8]. Consequently, the development of green synthetic methods for the MENPs can allow a persistent production of ultrapure nanoparticles with well-defined nano sizes (< 50 nm) as well as an even and firm anchoring on the carrier; however, to achieve such MENPs is one of the major challenges in nanotechnology [9]. Conventionally, wet-chemistry processes have been widely used to synthesize the MENPs. However, their scalability is limited by slow kinetics and batch operations, which typically result in an unpredictable variation in

the physicochemical properties of the MENPs. Moreover, the chemical precursors used during the synthesis can cause the contamination of the resulting nanomaterial surfaces, and harmful residual as well as by-product wastes can be released into the environment [10, 11]. Compared to chemical methods, pure physical procedures have significant advantages in the regularity of the production of nanoproducts. Thus far, multiple physical techniques, such as UV irradiation, lithography, laser ablation, ultrasonic fields, and photochemical reduction and spark ablation aerosol (SAA) technologies, have been successfully used to produce nanoparticles [9, 12-14]. Lithography is specifically used in top-down nanopatterning on metal templates, and laser ablation can only be applied on a few metals; herein, the MENPs need to be dispersed and collected in the liquid, which affects their quality [15, 16]. The SAA technology generates MENPs by spark-induced evaporation and subsequent condensation with all metals and some nonmetallic elements (if a simple substance form is stable under ambient temperature and pressure conditions). By operation under a continuous gas flow, non-agglomerated particles (singlets) can be produced ranging from atom clusters to particles of favorable size (0.2–50 nm) by tuning the operating conditions [17, 18]. By simply changing the gas-phase components (oxygen ratio), the synthesis of elementary substances and oxide MENPs can be easily achieved. However, hydroxide MENPs have not been synthesized by the SAA method to date.

The MENPs generated by the SAA method need to be anchored onto appropriate carriers to avoid agglomeration and the loss of volume during application[4, 19].

Anastasopol *et al*. [20] collected Mg–Ti nanocomposites with super hydrogen storage characteristics and primary particle sizes of 10–20 nm on a PVDF membrane, wherein the initial Mg–Ti nanocomposites accumulated on the surface of the membrane and further dispersion was required. Lee *et al*. [21] deposited SAA-generated Au nanoparticles (NPs) on an organic semiconductor to increase conductivity. Park *et al*. [22] used a pulse DC power source to directly spark-ablate and coagulate W as well as WO_3 nanocolloid nanoclusters in deionized (DI) water for their characterization; however, the prospective applications have not been discussed. Feng *et al*. [23] loaded SAA-generated Ag NPs onto textile materials (cotton, polyester, acrylic, and lyocell rayon) as antimicrobial dressing, which resulted in good dispersion and strong attachment of the MENPs on the textile surface. In contrast, the nanofiber material synthesized by electrospinning had a fiber diameter range of 50–1000 nm and a high porosity of the final nanofiber membrane, which had a significantly higher specific surface area and was useful for capturing more MENPs [24-26]. However, the use of electrospun nanofibers to enhance the diffusional deposition of SAA-generated MENPs and their performance have not yet been reported.

In this study, a scalable and green method to synthesize and anchor ultrapure $La(OH)_3$ MENPs using SAA technology and electrospinning techniques is introduced; consequently, the produced MENPs are applied as efficient phosphate adsorbents for water remediation. $La(OH)_3$ nanoparticles or nanorods (<50 nm) have been proven as efficient and safe phosphate binders [27-29]. Elementary La primary particles generated by SAA have been observed to be approximately 2-20 nm in

diameter and strongly reactant, owing to the effect of the nanoscale; further, these particles can easily oxidize with atmospheric molecules of O_2 and water vapor under ambient conditions [30]. After oxidation occurs, the hydration reaction of La_2O_3 singlet particles with water vapor is used to generate $La(OH)_3$ particles, which are then deposited on the surface of the electrospun nanofibers to form ultrapure $La(OH)_3$ nanoparticles by coalescence and anchoring. Based on the adsorbent properties, $La(OH)_3$ can be successfully integrated in the nanofiber and the removal of phosphates can be achieved in spite of a coexisting ion interference. This method is scalable by redesigning and combining the SAA and electrospinning equipment, which facilitates the mass production of not only the adsorbent with lanthanum compounds but also of any MENP-related material.

2. Materials and methods

2.1 Synthesis and deposition of $La(OH)_3$ MENPs

The La NPs were synthesized using a spark ablation nanoparticle generator (VSP-G1, VSPARTICLE B.V., Delft, The Netherlands) operating at 1.38 kV voltage and 8.1 mA current. In this process, one pair of cylindrical La electrodes (Diameter = 8 mm and a length of 30 mm) was placed in the holders inside the bottom bracket. These were facing each other and separated to form a gap of ca. 1 mm, through which a carrier gas (2% O_2, 98% N_2) at 10 L/min flowed perpendicularly. Pulsed sparks were formed in the gap between the two electrodes because of the electric gas breakdown. The sparks ablated the La electrodes to condense into La_2O_3 prime particles through the reaction of La and O_2. Then, the bypassed water vapor (65 □),

carried by the N_2 gas with a standard flow rate of 10 L/min, was injected after the formation of prime particles. The La_2O_3 prime particles were mixed homogeneously and hydrated with water vapor to form $La(OH)_3$ prime particles. The $La(OH)_3$ prime particles coagulated and deposited on 0.01 g of the prepared PAN electrospun nanofiber membrane (synthesis methods are presented in Supplementary Figure S1) on a commercial filter holder (47-mm in-line filter holder; Pall Corporation, Port Washington, New York, USA). The $La(OH)_3$ MENP-loaded nanofibers were collected after 15 min (results for the different loading times are included in Supplementary Figure S2) and placed in an oven at 200 □ to dry for 12 h. Thereafter, characterization measurements and phosphate adsorption tests were performed.

2.2 Loading concentration of $La(OH)_3$ MENPs and evaluation of uniformity

The loading concentrations of $La(OH)_3$ MENPs were determined by ICP-MS (7700x, Agilent Technologies, Inc., Santa Clara, California, United States). A $La(OH)_3$ MENP-loaded nanofiber membrane (0.1 g) was digested in 6 mL of cc. HCl and 2 mL of cc. HNO_3 (Guoyao Technology Co., Ltd., China) in a microwave digestion system (SP-1445, CEM, USA). The La contents of the digests were quantified using an ICP-MS instrument, and La standard solution ($La(NO_3)_3$ in 5 M HNO_3, 1000 mg/L, Sigma-Aldrich Corporation, St. Louis, Missouri, USA) was used to calibrate it. STA (DSC/DTA-TG, STA 449 F3, NETZSCH, Germany) was applied to test the accurate weight of the $La(OH)_3$ MENPs deposited on the fiber. The temperature was increased in the range of 100–1000 °C and the rate of increase was 10 □/min in a nitrogen atmosphere. To evaluate the uniformity of NP deposition

within the nanofiber, XPS-etching studies were performed on the sample with an etching time of 220 s (approximately 70.4 nm of etching depth per level on the PAN nanofiber) at each level for four levels.

2.3 Surface Chemistry Characterization

The surface morphologies of the samples of $La(OH)_3$ MENP-loaded nanofiber membranes were analyzed using FE-SEM (Hitachi S4800 and Phenom LE, Hitachi, Ltd., Tokyo, Japan) and EDS (Apollo XL, EDAX, USA). The particle size distribution was determined by counting all particle diameters of the ten SEM images (ca. 1000 particles) from different parts of the samples with the ImageJ™ 2.0 software. Detailed information regarding the structure of the $La(OH)_3$ MENPs found on the fibers was obtained by SAXS (SAXSess mc^2, Anton Paar, Austria). The Guinier–Porod empirical model was used to fit the SAXS scattering pattern [31]. The model is described by the equations shown below [31].

$$\mathrm{I(q)} = \mathrm{G} \cdot \exp\left(\frac{-q^2 R_g^2}{3-s}\right) \quad \text{for } \mathrm{q} \leq \mathrm{q_1} \tag{1}$$

$$\mathrm{I(q)} = \frac{D}{q^d} \qquad \text{for } \mathrm{q} \geq \mathrm{q_1} \tag{2}$$

$$\mathrm{q_1} = \frac{1}{R_g}\left(\frac{3d}{2}\right)^{\frac{1}{2}} \tag{3}$$

$$\mathrm{D} = \mathrm{G} \cdot \exp\left(-\frac{d}{2}\right)\left(\frac{3d}{2}\right)^{\frac{1}{2}} \frac{1}{R_g^d} \tag{4}$$

The scattering intensity is descripted by a piecewise function in equations 1 and 2. *q* represents the scattering variable, *I(q)* is the scattered intensity, R_g represents the radius of gyration, *d* represents the Porod exponent, *s* is a dimensional variable (the

higher the value of 3-*s*, the more spherical the particles), *G* is the Guinier scale factor, and *D* represents the Porod scale factor.

The analysis of the material phase patterns of $La(OH)_3$ MENP-loaded nanofiber membranes was conducted using XRD (Rigaku Ultimate IV diffractometer, Rigaku Corporation, Tokyo, Japan) with a high-power Cu Kα source, and a Bruker D8 Advance diffractometer was used in the 2θ range of 5–90°. MDI Jade 6.0 (Materials Data, Inc., Livermore, California, USA) was used to analyze the phase pattern of the XRD results to confirm the formation of $La(OH)_3$. Fourier transform infrared (FTIR) spectroscopy (Thermo Nicolet 6700, Thermo Fisher Scientific, Waltham, Massachusetts, USA) was also used to confirm the synthesis and adsorption of $La(OH)_3$.

A FEI TF20/2100F instrument (FEI Company, Hillsboro, Oregon, USA) was used to obtain high-resolution transmission electron microscopy (HR-TEM) images and selected-area diffraction pattern images with a 200 kV operating voltage. Plastic embedding frozen slicing is a new analysis method, which was incorporated for the inclusions of steel in this study by the electrolysis of nonaqueous solutions that have been associated with the RTO metal embedded cutting film micron-nano token method. A copper grid (Quantifoil R1.2/1.3 400) was used to collect the HR-TEM samples after the nanofiber plastic embedding frozen slicing. The results were analyzed using the DigitalMicrograph 9.2 software (Gatan, Inc., Pleasanton, California, USA).

XPS (Thermo Fisher Scientific, K-Alpha) was employed to confirm the presence and adsorption of $La(OH)_3$ in the generated MENPs. C 1s peak (284.8 eV) was used to calibrate the XPS results. A monochromatic Al Kα X-ray (1486.6 eV of photons) spectrum was used as the reading source. The NPs collected on the filter membranes were directly placed on the sample holder. The measurements were performed at a pass energy of 40 eV and a 0.05 -eV step size with the flood gun turned on.

2.4 Evaluation of Phosphorus adsorption on $La(OH)_3$ MENP-loaded nanofibers

The phosphorus binder adsorption efficiency evaluation batch tests have been fully described in a previous study [32]. In brief, the adsorption kindics (setting shown in Supplementary S5), equilibrium adsorption, and the coexisting ion interference in the 2-12 pH range of the materials were tested to study the adsorption pattern of $La(OH)_3$ MENP-loaded nanofibers. All the tests were condcuted in 250 ml erlenmeyer flasks, and 0.4g $La(OH)_3$ MENP-loaded nanofiber (mutiple pieces) (the $La(OH)_3$ MENP weight ratio in the materials was 10.5 % w/w; results shown in Supplementary Figure S4) was added in each treatment, which was repeated twice. The pure PAN fibers and $La(OH)_3$ nanoparticles P adsorption capacities were 0.00 and 65.5 mg P/g, respectively. Potassium dihydrogen phosphate (KH_2PO_4, Guoyao Technology Co., Ltd., China) was chosen as the phosphate source, and 0.4 g of $La(OH)_3$ MENP-loading nanofibers (10.5 % w/w, using the weighting process described in Supplementary Figure S4) was added to 100 ml phosphate in a flask for every test, wherein the pH of the solution was adjusted previously according to the test settings.

2.5 Durability of $La(OH)_3$ MENP-loaded nanofibers

The loss of $La(OH)_3$ MENPs and leaching from the nanofibers after application in water was tested to evaluate the durability. The sample (0.4 g) was added to 100 ml of 20 mg/L phosphate solution in a 250-ml flask. Heat-treated (200 □) $La(OH)_3$ MENP-loaded nanofibers, raw $La(OH)_3$ MENP-loaded nanofibers, and pure PAN nanofiber membranes (with duplications) were added and shaken for 60 min at 25 °C for three cycles. The La concentration was analyzed using ICP-MS to determine the content of $La(OH)_3$ MENPs embedded in the textiles (mg/kg).

3. Results and discussion

3.1 Surface chemistry and material characterization

X-ray diffraction (XRD) results of blank (La prime particle, N_2 carry gas, water vapor added) and treated (La prime particle, 98% N_2 + 2% O_2 carry gas, water vapor added) nanofiber samples are presented in Figure 1A. Based on the diffraction peaks observed and the JCPDS index, the diffraction peaks for the La prime particle with different treatments revealed a hexagonal phase (JCPDS 40-1284) and the three key peaks with 2θ values of 28.12, 39.50, and 48.8 corresponded to the (110), (002), and (211) planes of the crystalline La_2O_3. For the La_2O_3 prime particle samples, all the observed diffraction peaks indicated a pure hexagonal phase (JCPDS 06-0585) of $La(OH)_3$ with a=6.528 Å and c=3.858 Å as the lattice constants, and 13 main peaks were detected between 10° and 80° corresponding to the (100), (101), (110), (201), (210), (002), (211), (300), (220), (310), (302), (222), and (312) crystalline $La(OH)_3$ planes. These results indicate that the La prime particle cannot be hydroxylated with water vapor in this system; however, the La_2O_3 prime particle is observed to easily

hydroxylate with water to generate $La(OH)_3$ in this airtight system. To elucidate the reason for the La prime particle-loaded nanofiber exhibiting La_2O_3, Fourier transform infrared (FTIR) spectra of the as-prepared SAA-generated La_2O_3 (La prime particle with water vapor) and $La(OH)_3$ (La_2O_3 prime particle with water vapor) samples are shown in Figure 1B. Compared to the FTIR spectrum of samples with La + water vapor, the $La(OH)_3$ generated by La_2O_3 + water vapor showed the typical peaks for La-O-H and O-H of $La(OH)_3$. The band at 3605 cm^{-1} can be qualified to the vibration of the -OH groups of $La(OH)_3$ [33]. The two bands at 3440 cm^{-1} and 1635 cm^{-1} match O–H vibrations [34]. The bands at approximately 649.6 cm^{-1} correspond to the bending vibration of La–O–H [35]. These data sets confirm that the hydroxylation of the prime nano La_2O_3 to $La(OH)_3$ is rapid and complete under moderate conditions (45 □). The speed of the reaction can be attributed to the strong basicity of La_2O_3 under airtight conditions. The reaction with water in the gas phase is significantly easier when the particle is in a unit digit nanoscale. Prior reports have suggested that the same reaction can only occur at 1073–1273 K with a reaction time of 8 h if La_2O_3 is not in the nanoscale [30]. The survey X-ray photoelectron spectroscopy (XPS) spectra of both samples also confirm that $La(OH)_3$ MENPs were successfully synthesized and loaded in the La_2O_3 prime particle sample. Figure 1C shows that the XPS data is in accordance with the La_2O_3 and $La(OH)_3$ spin-orbit pattern. In the La_2O_3 + vapor results, the typical La $3d_{5/2}$ and $3d_{3/2}$ XPS peaks were detected at 835.08 and 851.98 eV with *Δu"* of 16.9 eV. Contrarily, the La $3d_{5/2}$ and $3d_{3/2}$ peaks of La + vapor samples were observed to have higher binding energies than that of La_2O_3

+ vapor with 836.51 ($\Delta v'$ to $La(OH)_3$ MENPs was 1.43) and 853.31 eV ($\Delta v''$ to $La(OH)_3$ MENPs was 1.33) and the spin-orbit split was 16.8 eV($\Delta u'$) [35]. The results prove that the SAA technology is a green and efficient method to produce $La(OH)_3$ MENPs, as compared to the wet chemistry synthesis method.

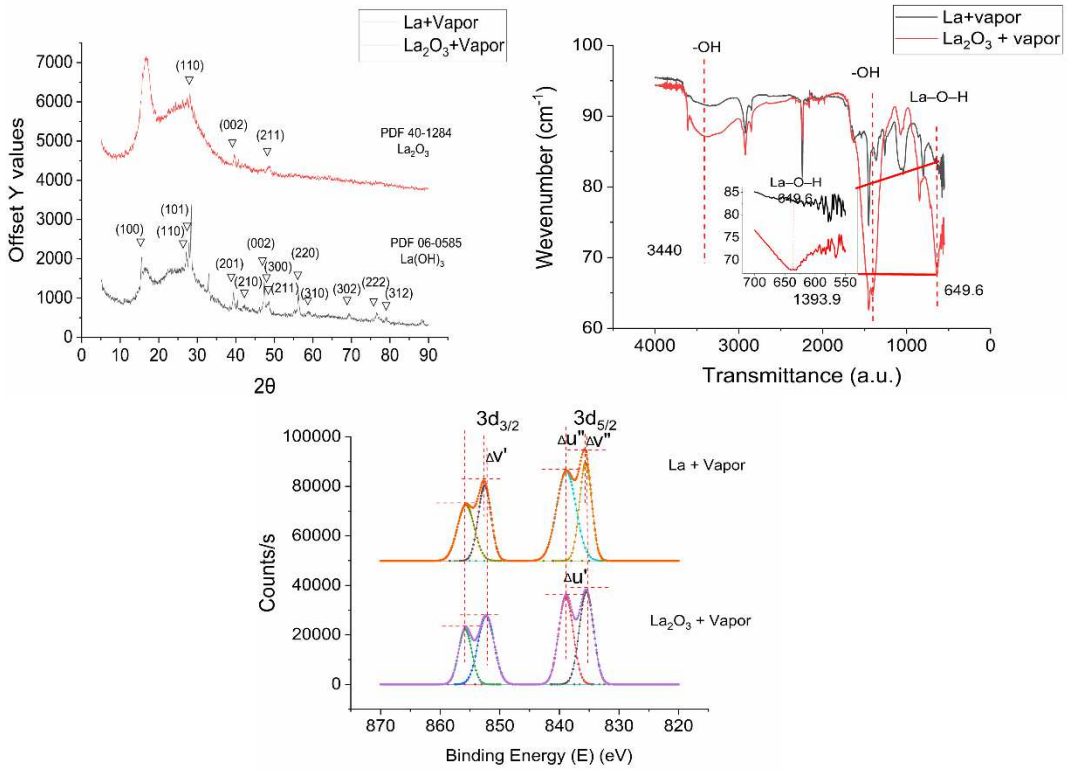

Figure 1. (A) XRD patterns of the La prime particle-loaded (N_2 carrier gas, reacted with water vapor) and La_2O_3 prime particle-loaded (98% N_2 + 2% O_2 carry gas, reacted with water vapor) nanofiber samples. (B) FTIR spectra and (C) high-resolution XPS La 3d spectra of the La prime particle-loaded and La_2O_3 prime particle-loaded nanofiber samples.

3.2 Morphology, particle size distribution, and deposition efficiency

Field-emission scanning electron microscopy (FE-SEM) was used to observe the morphology and general size distribution of the $La(OH)_3$ MENPs generated using the SAA method. Figures 3A and 3B show the SEM images of the $La(OH)_3$ MENPs on the PAN nanofibers (the properties of PAN nanofibers are shown in Figure S1) before and after the heat treatment. The $La(OH)_3$ MENPs are scattered on the nanofiber surface. During deposition, the majority of these are deposited as a singlet, whereas few are clustered(Figure 2A); this is because of the van der Waals contact force and electrostatic effect of the existing particles. The singlet MENP deposition is highly desirable, as singlets can strongly adhere to the nanofibers as compared to the agglomerates. After heat treatment at 200 □, the fluffy cluster collapsed and the MENPs bound on the nanofiber surface were more compact. This is because the thermal treatment can “sinter” the nanoparticles on the nanofiber; “sintering nanoparticles on the nanofiber” increases the contact area of the nanoparticles and the fiber material (which increases the van der Waals contact force). This is because the thermoplastic fiber material becomes soft, enabling a better imbedding of the particles in the fiber material that comprises a low melting point (PAN melting point is 260 □). Figure 2C shows that the size distribution of the $La(OH)_3$ MENPs compacted agglomerates followed a log-normal distribution ($p=0.328 > 0.05$, AD = 0.417) based on the diameters of 1000 MENPs that were measured by the ImageJ™ software. The mean diameter and standard deviation of the observed $La(OH)_3$ MENPs were 15.4 nm and 1.8. These results show that the $La(OH)_3$ MENPs loaded on nanofibers have a uniform size and they were effectively loaded on the nanofiber. EDS mapping results

are shown in Figures 2D, 2E, and 2F. These results show that the La elemental distribution can be suitably overlain with the C elemental (nanofiber framework) distribution, which proves that the SAA-generated $La(OH)_3$ MENPs are uniformly deposited on the nanofiber. These results were confirmed by the TEM results shown in Figures 2G, 2H, and 2I. The resin embedding frozen slicing of a vertical section of the $La(OH)_3$ MENPs loading nanofiber can be observed in Figure 2G. Evidently, the $La(OH)_3$ MENPs are uniformly loaded around the nanofibers, and particle embedding can also be seen in Figure 2H. Moreover, the majority of $La(OH)_3$ MENPs on nanofibers remained as singlets (Figure 2I), which indicates that this method effectively reduced the agglomeration of MENPs. The EDS mapping and selected area electron diffraction results of the vertical section are shown in Figure S3, which confirm that the $La(OH)_3$ MENPs were successfully synthesized and loaded on elcectrospun nanofibers.

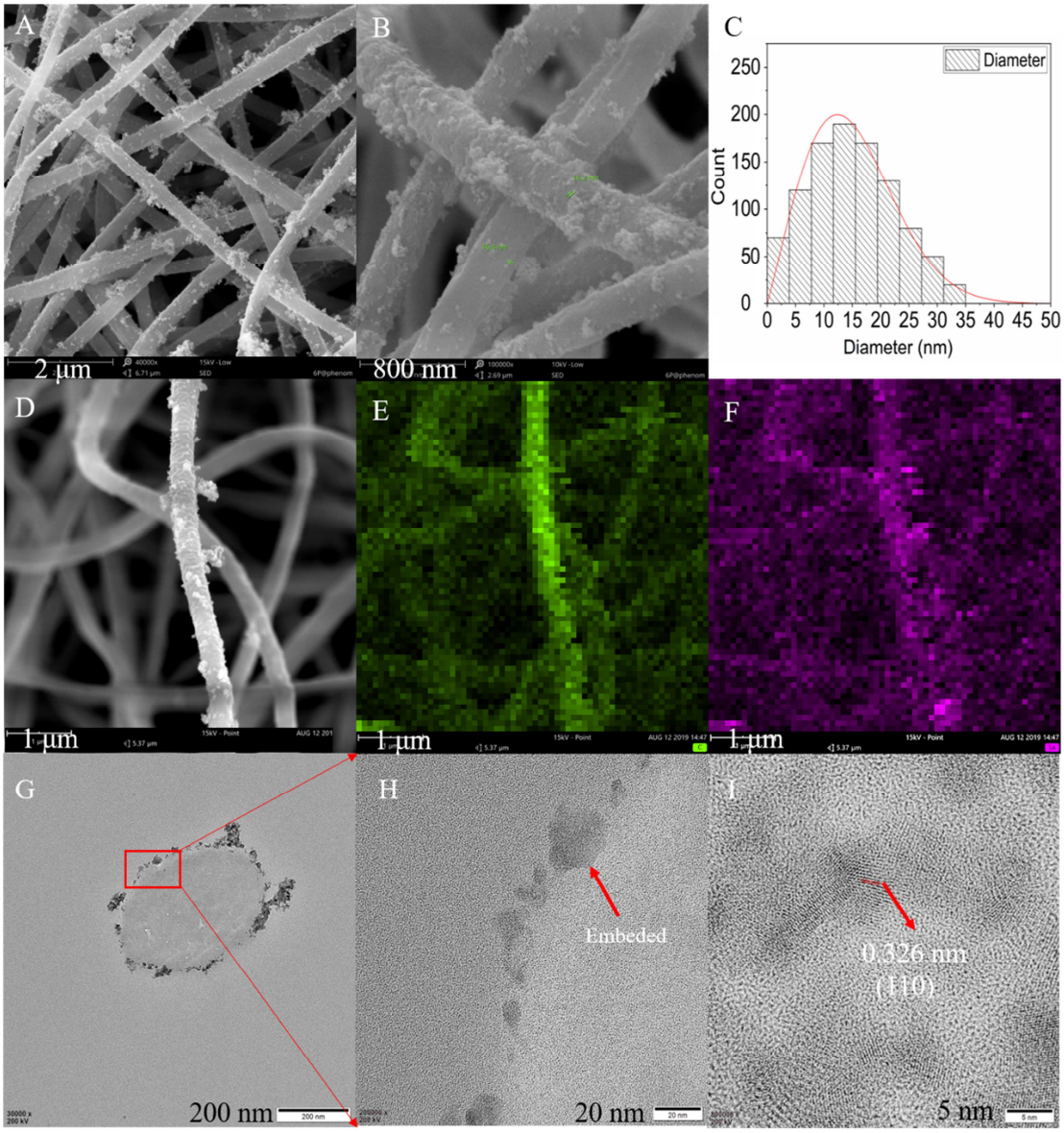

Figure 2. (A) Scanning electron microscopy (SEM) image of a $La(OH)_3$ MENP-loaded nanofiber (fiber diameter of 150–300 nm). (B) SEM image of a $La(OH)_3$ MENP-loaded nanofiber after heat treatment at 200 □. (C) Particle size distribution based on the SEM image. (D) FEG-SEM image and elemental mapping of a $La(OH)_3$ MENP-loaded nanofiber. (E) C and (F) La element distributions. (G) Transmission electron microscope (TEM) image of resin embedding frozen slicing of

a $La(OH)_3$ MENP-loaded nanofiber. (H) TEM image of the cross-section between a $La(OH)_3$ MENP and a nanofiber (I) TEM image of a $La(OH)_3$ MENP singlet .

The deposition efficiency of the $La(OH)_3$ MENPs onto the nanofibers depends on the ablation rate of La [36], flow rate of the carrier gas, and nanofiber characteristics. The above-mentioned ablation rate is based on the operating voltage and current; further, the La ablation rate and the La generation rate in this study was 0.51 nmol/J and 0.000715 g/15 min, respectively. The La concentration deposited on the nanofibers (0.01 g, each piece) was 6.89 % (measured by ICP-MS), and 97.8% of the La element was filtered and trapped by the nanofibers; further, the final mass ratio of $La(OH)_3$ loaded on the nanofibers was 10.5 % (measured by STA as shown in Supplementary Figure S5). Based on the XRD result, the membrane surface did not exhibit La_2O_3 peaks and 99.9 % of the La prime particles generated by the SAA method could be transformed to $La(OH)_3$; this led to a good synthetic yield. The probable reason for the high yield is that the bypass water vapor flux facilitates the vapor and La particles to mix more uniformly. The porous steel strap-supporting plate for the membrane in the holder might also be responsible as it helps to trap more particles inside the membrane.

3.3 Evaluation of the uniformity of particle deposition

The primary particle size and surface properties of the $La(OH)_3$ MENPs were determined by SAXS and the results are shown in Figures 4A and 4B. The scattering intensity *I* of the pure PAN nanofiber and $La(OH)_3$ MENP-loaded nanofibers can be

calculated by the equation $q = (4\pi\sin\theta)/\lambda$ based on the 2θ or scattering vector recorded. Figure 3A shows the SAXS data for the $La(OH)_3$ MENP-loaded nanofibers. The Guinier–Porod empirical model fits with the SAXS scattering data with $R^2 = 0.99$. The results show that the scattering intensity followed a negative biquadrate power law with the scatter variable ($I \propto q^{-4}$), where q ranges (0.5 to 2 nm^{-1}) dropped in the Porod law section, which indicates that the $La(OH)_3$ MENPs had a smooth surface with a Porod exponent of d=3.85 ≈ 4 , which revealed a less agglomerated surface [34]. When q was less than 0.5 nm^{-1} (Guinier law), R_g (gyration radius) for the $La(OH)_3$ MENPs was 14.3 nm, close to a mean diameter d_p of 18.5 nm, which was measured above by the SEM [23]. The 3-s (Sphericity) value was equal to 3, which indicates that the $La(OH)_3$ MENPs are globular or spherical [37]. As shown in Figure 2B, the real-space distance distribution function is curved, and the results show that the general distance between the two points matches the particle diameter of 18.5 nm.

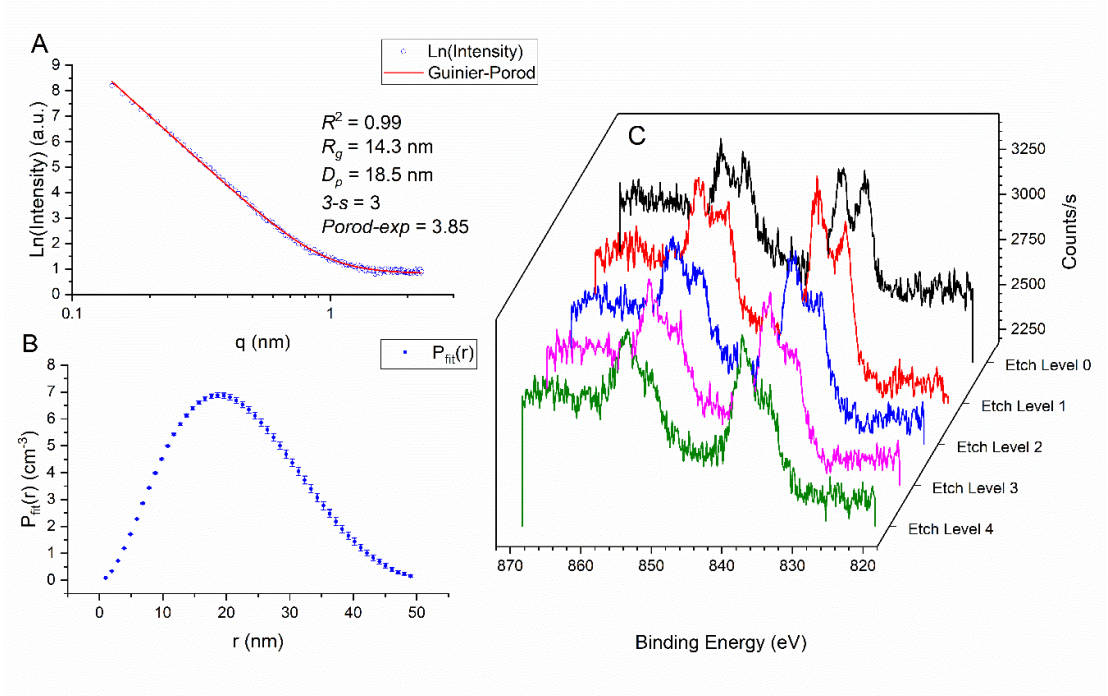

Figure 3. Small angle X-ray scattering (SAXS) and X-ray photoelectron spectroscopy etching measurements for a $La(OH)_3$ MENP-loaded nanofiber. (A) SAXS data with Guinier–Porod empirical model fitting and (B) real-space distance distribution function fitting. (C) Depth profile of a $La(OH)_3$ MENP-loaded nanofiber of the XPS etching test (the etching level was four, the etching time was 220 s, and the beam energy was 1000 eV).

Figure 3C shows the XPS spectra of a $La(OH)_3$ MENP-loaded nanofiber etched with 1000 eV beam energy as a function of etching time. Before etching, the peak energies and shapes of La $3d_{3/2}$ and La $5d_{3/2}$ corresponded to those for $La(OH)_3$ [38]. After etching for 220 s, the peak positions and shapes of La $3d_{3/2}$ (851.98 eV) and La $5d_{3/2}$ (835.08 eV) exhibited no changes [39]. The results for the intensity counts of each etching layer showed a smaller reduction from the front surface to the deep layers, even with 70-nm depth per layer etching. This result reveals that the electrospun nanofiber can not only effectively trap the SAA-generated NPs, but also shows a uniform 3D $La(OH)_3$ MENP deposition inside the nanofiber membrane.

3.4 Phosphorus adsorption on $La(OH)_3$ MENP-loaded nanofibers

In figure 4A, the $La(OH)_3$ MENP-loaded nanofibers show good performance in the entire pH range on phosphate adsorption (> 80.7 mg P/g La); however, the adsorption capacities increased more at a low pH range of 3–7 (higher than 100.0 mg P/g La) than at a high pH of 9–12. Ligand exchange was addressed as the main mechanism of this result. This was due to the fact that at low pH, more H^+ are involved and attach

with $La(OH)_3$ to attract the negatively charged ions of PO_4^{3-}, HPO_4^{2-}, and $H_2PO_4^-$. On the contrary, under high pH conditions (9-12), the exchange probability of -OH on $La(OH)_3$ with PO_4^{3-}, HPO_4^{2-}, and $H_2PO_4^-$ rapidly reduces, thereby decreasing the adsorption capacity of the $La(OH)_3$ MENP-loaded nanofiber. Figure 1B illustrates the fitting curves of the Langmuir and Freundlich equilibrium adsorption isotherms of the $La(OH)_3$ MENP-loaded nanofibers, the fitting equations are presented in Table S5. The results show that both the Freundlich ($R^2 = 0.96$) and Langmuir model ($R^2 = 0.95$) are well fitted to the isotherm. K_f and n values are both considerably higher than 1 for the Freundlich model, suggesting a robust interaction between $La(OH)_3$ MENP-loaded nanofibers and the phosphates. However, q_0 is measured as 110.8 mg P/g La, which is substantially greater than that for the non-loaded $La(OH)_3$ nanoparticles. The likely reason for these patterns is that the well scattered $La(OH)_3$ MENPs on nanofibers contribute to a more surface active $La(OH)_3$ adsorption core for the binding of phosphates and a smaller aggregation potential when applied in water [32]. The phosphate adsorption equilibrium time and $La(OH)_3$ MENP-loaded nanofiber adsorption kinetics pattern are shown in Figure 4C. The phosphate adsorption on the adsorbent reached the equilibrium after 24 h (1,440 min) of testing. However, the test concentration of the phosphate dropped rapidly from 0 to 60 min, and about 80% of the initial concentration would have been removed during this period. The findings of the ANOVA analysis indicate that there were no significant differences between each replication (p 0.05), suggesting strong reproducibility. Thereafter, the pseudo first-order equation, pseudo-second-order (PSO) equation, and

exponential equations were fitted to determine the adsorption kinetics of the $La(OH)_3$ MENP-loaded nanofibers, the fitting equation and results of which are included in Tables S5 and S6. In addition, the goodness of fit was evaluated by the R^2 value and the standard deviation. From the results, the PSO equation showed the best goodness of fit as compared to the other equations ($R^2 \geq 0.99$). Moreover, the adsorption rate constant K_2 for the initial 20, 50, and 100 mg/L tests were 0.012, 0.0083, and 0.001, respectively. Based on the PSO equation theory, a lower K_2 value designates a shorter half-life of the reactant (half adsorption capacity used). Meanwhile, the PSO equation driven reaction was sensitive to the value of the initial concentration, which reveals that $La(OH)_3$ MENP-loaded nanofibers would remove phosphate faster under higher initial concentrations. Furthermore, the smaller $La(OH)_3$ MENP diameter also boosts the absorption process because the chemisorption process (impacted by active site volume and exposure; the hydroxyl on $La(OH)_3$ would exchange with PO_4^{3-}, HPO_4^{2-}, and $H_2PO_4^-$ to form a ionic bond) is involved when the PSO kinetics equation dominated. Figure 1D shows the effects of the coexisting ions under various pH conditions. The adsorption efficiency of $La(OH)_3$ MENP-loaded nanofibers was affected by co-existing ions, but it showed a high performance of adsorption selectivity for phosphate, and pH effects on adsorption shared the same patterns in Figure 1A. In a pH range between 3-7, the average coexisting ion (F^-, NO_3^- SO_4^{2-}, and Cl^-) adsorption rate of $La(OH)_3$ MENP-loaded nanofibers was 4.81 mg/g and 1.05 mg/g at pH 9–13. The ion exchange affinity order of those coexisting ions is the key factor to impact the adsorption selectivity of $La(OH)_3$ MENP-loaded nanofibers on

phosphate. A better ion affinity indicated an easier binding with adsorbents (the solubility of their La compounds also contributed to this result) but the adsorption of the ion occurred mainly by the ligand exchange of OH^- [40]. In general, the ligand exchange of OH^- dominated the adsorption process, and the $LaPO_4$ crystallized along with the (1 1 0) plane of $La(OH)_3$ and ultimately grew on the surface of the $La(OH)_3$ nanoparticles and nanofibers. More details about the mechanisms of PO^{4-} adsorption on $La(OH)_3$ loaded nanofiber membranes can be found in our previous studies [32].

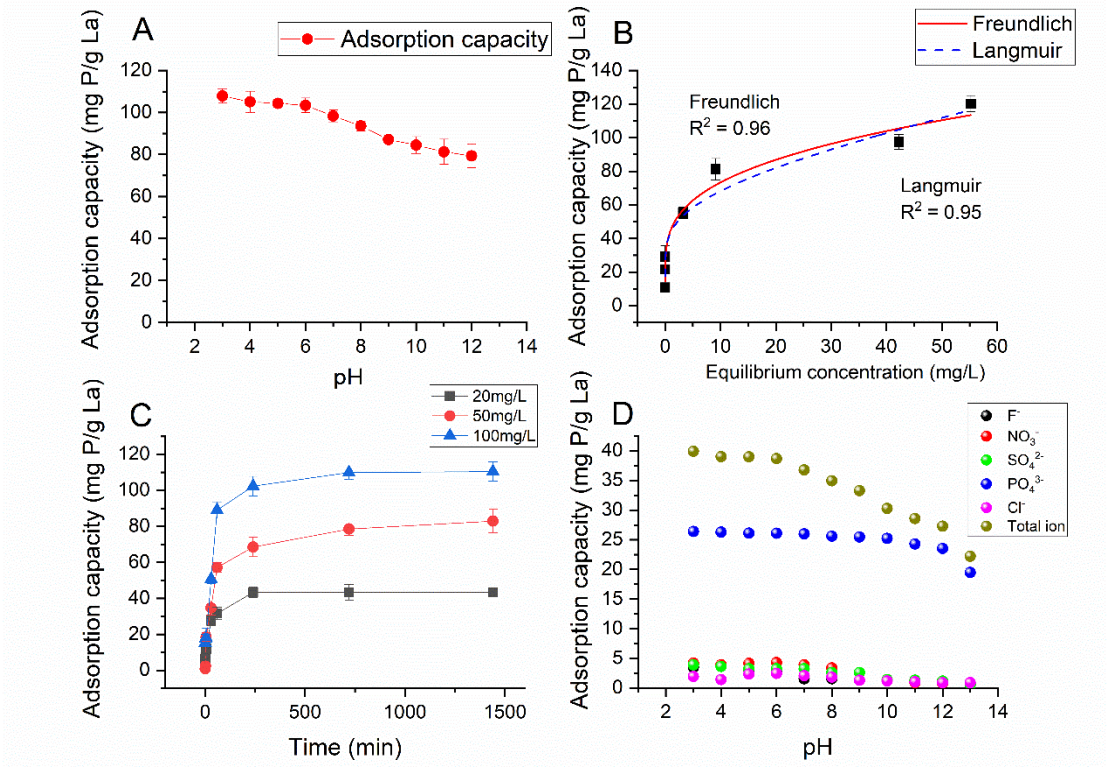

Figure 4. (A) Effect of pH on the phosphate adsorption on $La(OH)_3$ MENP-loaded nanofibers. (B) Adsorption isotherms for phosphate adsorption on $La(OH)_3$ MENP-loaded nanofibers (initial concentrations of 10, 20, 50, 100, 150, 200, and 250 mg P/L). (C) Kinetics of phosphate adsorption on $La(OH)_3$ MENP-loaded nanofibers (initial concentrations of 20, 50, and 100 mg P/L). (D) Affinity of various anions

toward $La(OH)_3$ MENP-loaded nanofiber adsorbent (the concentration of each anion was 2.0 mmol/L).

3.5 Durability and recycling of $La(OH)_3$ MENP-loaded nanofibers for water treatment

When the $La(OH)_3$ MENP-loaded nanofibers are applied to treat water, the falling-off rate for the $La(OH)_3$ MENPs and durability should be considered. To evaluate the loss-rate of the $La(OH)_3$ MENPs from the nanofiber, a mechanical shaking test was carried out. The results (Figure 5) show that the non-heated sample exhibited a higher loss of the $La(OH)_3$ MENPs compared to that for the heat-treated sample. In the first shaking cycle, 27.8 wt% of $La(OH)_3$ MENPs in the non-heated sample fell off. Comparatively, only 6.44 wt% of $La(OH)_3$ MENPs on the pre-heated sample were lost during the shaking test. The losses for both the non-heated and heated samples were dramatically reduced after the second cycle (7.4 wt% for the non-heated sample and 1.8 wt% for the heated sample). A likely reason for this result is the over-deposition and agglomeration (Figure 1A) of the MENPs detached during the first shaking process [20]. During the third shaking test, 5.9 wt% of $La(OH)_3$ MENPs in the non-heated and 0.53 wt% of $La(OH)_3$ MENPs in the heated samples were lost. In this case, the loss in the heated sample decreased to less than ca. 1.0 wt%, which is acceptable. The deposition of MENPs within the nanofiber membrane (Figure 3C) reduces their release during the application. The particle size is an additional important parameter that affects the adhesive strength. If the diameter becomes smaller, the contact van der Waals force becomes larger relative to the drag

force within the boundary layer or the inertial force during shaking. Moreover, the recovery of MENPs nanofiber membranes was also tested, and the results are shown in Supplementary Figures S7 and S8. The results show that the membrane could maintain the phosphate adsorption capacity of at least 80 mg P/g La after three recovery cycles. Meanwhile, comparisons with other super phosphate adsorbents have been made, and the results are shown in Supplementary Table S9. However, this material cannot be regarded as an adsorbent with the highest efficiency, as compared to other materials; meanwhile, with regard to synthesis costs, time, and side effects, this material is the most suitable.

Another concern regarding the leaching of NPs is human and environmental safety. Although La compounds are known to have a smaller toxicity for humans and animals (these can be used as a medicine to cure the kidney disease), the side-effects of nano La particles are not known [41]. Additional techniques need be developed to address this issue. Another possible method is the deposition of the SAA-generated MENPs along with the electrospinning process. If MENPs can be loaded on the nanofiber surface before the solvent evaporates from the fiber material, solvent evaporation takes place when nanoparticles are already present, and this may increase the contact area between the particles and the fiber. This is, for example, because solvent evaporation makes the particles mobile and lets agglomerates reform, so that they find more contact points on the fiber (reducing the total surface free energy). However, further studies are needed to support this hypothesis.

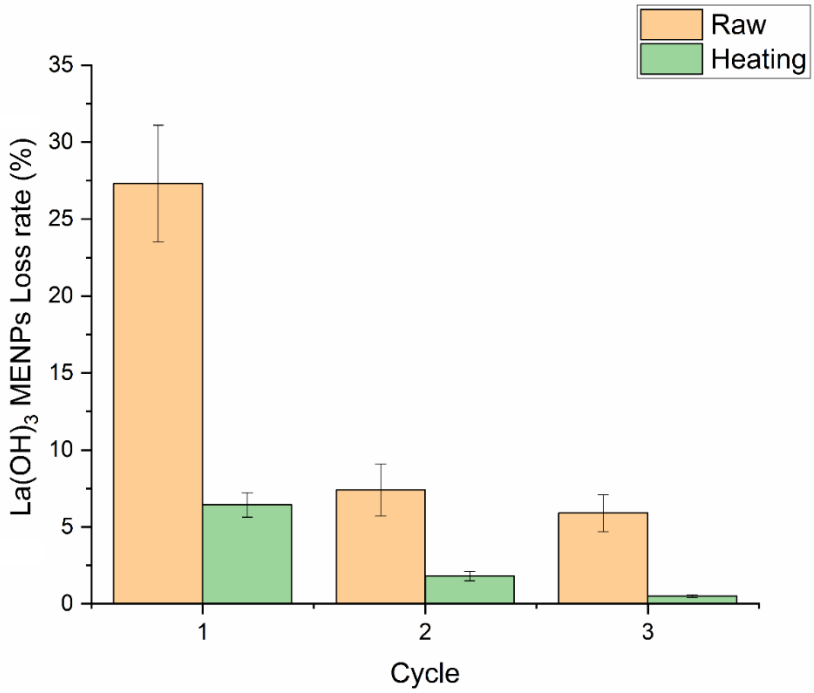

Figure 5. Durability of $La(OH)_3$ MENP-loaded nanofibers for water treatment

4. Conclusions

The presented method can effectively shorten and purify the synthesis as well as the loading of $La(OH)_3$ MENPs with reduced NPs agglomeration. The loading of $La(OH)_3$ MENPs on the electrospun nanofibers was uniform in both two and three dimensions. The phosphate adsorption results show that the $La(OH)_3$ MENP-loaded nanofiber formation is ideal to remove phosphates considering their removal efficiency, simple and easy operating as well as handling, and no sludge generation. Heating was found to be an effective anchoring method to immobilize the MENPs on the nanofiber; however, better anchoring techniques are still necessitated. This MENP loading method is not limited to La or adsorbent synthesis, and can also be applied to

catalysis, energy conversion and storage, sensors, and related applications. Furthermore, because of their anchoring properties, the nanofiber structures are easy to apply or assemble for practical use. Although further studies and input on more useful applications are required for further improvements, the proposed technique is extremely promising.

Acknowledgment

We gratefully acknowledge the National Science Foundation of China [Grant No. 51809195], Postdoctoral Science Foundation of China [Grant No. 2018M642083], National Water Pollution Control and Treatment Science and Technology Major Project of China [Grant Nos. 2017ZX07204004, 2017ZX07204002]

References

[1] R. Xu, M. Zhang, R.J.G. Mortimer, G. Pan, Enhanced Phosphorus Locking by Novel Lanthanum/Aluminum–Hydroxide Composite: Implications for Eutrophication Control, Environ. Sci. & Technol. 51 (2017) 3418-3425.

[2] Y. Zhang, B. Pan, C. Shan, X. Gao, Enhanced Phosphate Removal by Nanosized Hydrated La(III) Oxide Confined in Cross-linked Polystyrene Networks, Environ. Sci. & Technol. 50 (2016) 1447-1454.

[3] L. Fang, Q. Shi, J. Nguyen, B. Wu, Z. Wang, I.M.C. Lo, Removal Mechanisms of Phosphate by Lanthanum Hydroxide Nanorods: Investigations using EXAFS,

ATR-FTIR, DFT, and Surface Complexation Modeling Approaches, Environ. Sci. & Technol. 51 (2017) 12377-12384.

[4] A.M. Ealias, M. Saravanakumar, A review on the classification, characterisation, synthesis of nanoparticles and their application, IOP Conf. Ser. Mater. Sci. Eng, 2017, pp. 032019.

[5] N. Hoshyar, S. Gray, H. Han, G. Bao, The effect of nanoparticle size on in vivo pharmacokinetics and cellular interaction, Nanomedicine 11 (2016) 673-692.

[6] M. El-Shall, A. Edelstein, Formation of clusters and nanoparticles from a supersaturated vapor and selected properties, Institute of Physics: Philadelphia, 1996, pp. 13-20.

[7] P. Reineck, D. Brick, P. Mulvaney, U. Bach, Plasmonic Hot Electron Solar Cells: The Effect of Nanoparticle Size on Quantum Efficiency, J. Phys. Chem. Lett. 7 (2016) 4137-4141.

[8] T.L. Tan, L.-L. Wang, J. Zhang, D.D. Johnson, K. Bai, Platinum Nanoparticle During Electrochemical Hydrogen Evolution: Adsorbate Distribution, Active Reaction Species, and Size Effect, ACS Catal. 5 (2015) 2376-2383.

[9] O.V. Kharissova, H.V.R. Dias, B.I. Kharisov, B.O. Pérez, V.M.J. Pérez, The greener synthesis of nanoparticles, Trends Biotechnol. 31 (2013) 240-248.

[10] M.A. Schmidt, D.Y. Lei, L. Wondraczek, V. Nazabal, S.A. Maier, Hybrid nanoparticle-microcavity-based plasmonic nanosensors with improved detection resolution and extended remote-sensing ability, Nat. Commun. 3 (2012).

[11] F.E. Kruis, H. Fissan, A. Peled, Synthesis of nanoparticles in the gas phase for electronic, optical and magnetic applications—a review, J. Aerosol Sci. 29 (1998) 511-535.

[12] H.-J. Hwang, K.-H. Oh, H.-S. Kim, All-photonic drying and sintering process via flash white light combined with deep-UV and near-infrared irradiation for highly conductive copper nano-ink, Sci. Rep. 6 (2016) 19696.

[13] C. Huang, M.F. Becker, J.W. Keto, D. Kovar, R. S., P. V., A. D., Annealing of nanostructured silver films produced by supersonic deposition of nanoparticles, J. Appl. Phys. 102 (2007) 054308.

[14] S. Linic, U. Aslam, C. Boerigter, M. Morabito, Photochemical transformations on plasmonic metal nanoparticles, Nat. Mater. 14 (2015) 567.

[15] M. Ullmann, S.K. Friedlander, A. Schmidt-Ott, Nanoparticle Formation by Laser Ablation, J. Nanopart. Res. 4 (2002) 499-509.

[16] T.R. Jensen, M.D. Malinsky, C.L. Haynes, R.P. Van Duyne, Nanosphere Lithography: Tunable Localized Surface Plasmon Resonance Spectra of Silver Nanoparticles, J Phys. Chem. B 104 (2000) 10549-10556.

[17] J. Feng, G. Biskos, A. Schmidt-Ott, Toward industrial scale synthesis of ultrapure singlet nanoparticles with controllable sizes in a continuous gas-phase process, Sci. Rep. 5 (2015) 15788.

[18] J. Feng, L. Huang, L. Ludvigsson, M.E. Messing, A. Maisser, G. Biskos, A. Schmidt-Ott, General Approach to the Evolution of Singlet Nanoparticles from a Rapidly Quenched Point Source, J Phys. Chem. C 120 (2016) 621-630.

[19] C.-c. Jiang, Y.-k. Cao, G.-y. Xiao, R.-f. Zhu, Y.-p. Lu, A review on the application of inorganic nanoparticles in chemical surface coatings on metallic substrates, RSC Adv. 7 (2017) 7531-7539.

[20] A. Anastasopol, T.V. Pfeiffer, J. Middelkoop, U. Lafont, R.J. Canales-Perez, A. Schmidt-Ott, F.M. Mulder, S.W.H. Eijt, Reduced Enthalpy of Metal Hydride Formation for Mg-Ti Nanocomposites Produced by Spark Discharge Generation, J. Am. Chem. Soc. 135 (2013) 7891-7900.

[21] J. Lee, H. Kim, K. Han, Y. Lee, M. Choi, C. Kim, Controlled Enhancement in Hole Injection at Gold-Nanoparticle-on-Organic Electrical Contacts Fabricated by Spark-Discharge Aerosol Technique, ACS Appl. Mater. Interfaces 11 (2019) 6276-6282.

[22] K.-T. Park, M.M. Farid, J. Hwang, Anti-agglomeration of spark discharge-generated aerosols via unipolar air ions, J. Aerosol Sci. 67 (2014) 144-156.

[23] J. Feng, E. Hontañón, M. Blanes, J. Meyer, X. Guo, L. Santos, L. Paltrinieri, N. Ramlawi, L.C.P.M.d. Smet, H. Nirschl, F.E. Kruis, A. Schmidt-Ott, G. Biskos, Scalable and Environmentally Benign Process for Smart Textile Nanofinishing, Appl. Mater. Interfaces 8 (2016) 14756-14765.

[24] Y.C. Ahn, S.K. Park, G.T. Kim, Y.J. Hwang, C.G. Lee, H.S. Shin, J.K. Lee, Development of high efficiency nanofilters made of nanofibers, Curr. Appl Phys. 6 (2006) 1030-1035.

[25] K. Graham, M. Ouyang, T. Raether, T. Grafe, B. McDonald, P. Knauf, Polymeric nanofibers in air filtration applications, 5th annual technical conference & expo of the American Filtration & Separations Society, Galveston, Texas, 2002.

[26] X. Wang, K. Kim, C. Lee, J. Kim, Prediction of air filter efficiency and pressure drop in air filtration media using a stochastic simulation, Fibers Polym. 9 (2008) 34-38.

[27] L. Chen, Y. Li, Y. Sun, Y. Chen, J. Qian, $La(OH)_3$ loaded magnetic mesoporous nanospheres with highly efficient phosphate removal properties and superior pH stability, Chem. Eng. J. 360 (2019) 342-348.

[28] M.H. Gajewska, M. Kasprzyk, Preliminary results from application PHOSLOCK® to remove phosphorus compounds from wastewater, J. Ecol. Eng. 18 (2017) 82-89.

[29] Q. Mu, T. Chen, Y. Wang, Synthesis, characterization and photoluminescence of lanthanum hydroxide nanorods by a simple route at room temperature, Nanotechnology 20 (2009) 345602.

[30] P. Fleming, R.A. Farrell, J.D. Holmes, M.A. Morris, The Rapid Formation of $La(OH)_3$ from La_2O_3 Powders on Exposureto Water Vapor, J. Am. Ceram. Soc. 93 (2010) 1187-1194.

[31] B. Hammouda, A new Guinier-Porod model, J. Appl. Crystallogr. 43 (2010) 716-719.

[32] S. Li, X. Huang, J. Liu, L. Lu, K. Peng, R. Bhattarai, PVA/PEI crosslinked electrospun nanofibers with embedded $La(OH)_3$ nanorod for selective adsorption of high flux low concentration phosphorus, J. Hazard. Mater. 384 (2020) 121457.

[33] Q. Mu, Y. Wang, Synthesis, characterization, shape-preserved transformation, and optical properties of $La(OH)_3$, $La_2O_2CO_3$, and La_2O_3 nanorods, J. Alloys Compd. 509 (2011) 396-401.

[34] J.-G. Kang, Y.-I. Kim, D. Won Cho, Y. Sohn, Synthesis and physicochemical properties of $La(OH)_3$ and La_2O_3 nanostructures, Mater. Sci. Semicond. Process. 40 (2015) 737-743.

[35] M. Aghazadeh, B. Arhami, A.-A. Malek Barmi, M. Hosseinifard, D. Gharailou, F. Fathollahi, $La(OH)_3$ and La_2O_3 nanospindles prepared by template-free direct electrodeposition followed by heat-treatment, Mater. Lett. 115 (2014) 68-71.

[36] F. Braams, A Clean and Flexible Catalyst Synthesis Method: Metal nanoparticles on a fractal-like nanostructured metal oxide support, Master Dissertation, Delft University of Technology, Delft, The Netherlands (2015).

[37] G. Beaucage, Approximations Leading to a Unified Exponential/Power-Law Approach to Small-Angle Scattering, J. Appl. Crystallogr. 28 (1995) 717-728.

[38] J.P.H. Li, X. Zhou, Y. Pang, L. Zhu, E.I. Vovk, L. Cong, A.P. van Bavel, S. Li, Y. Yang, Understanding of binding energy calibration in XPS of lanthanum oxide by in situ treatment, Phys. Chem. Chem. Phys. 21 (2019) 22351-22358.

[39] B. Tang, J. Ge, C. Wu, L. Zhuo, J. Niu, Z. Chen, Z. Shi, Y. Dong, Sol–solvothermal synthesis and microwave evolution of $La(OH)_3$ nanorods to La_2O_3 nanorods, Nanotechnology 15 (2004) 1273-1276.

[40] Y.G. Ko, T. Do, Y. Chun, C.H. Kim, U.S. Choi, J.-Y. Kim, CeO_2-covered nanofiber for highly efficient removal of phosphorus from aqueous solution, J. Hazard. Mater. 307 (2016) 91-98.

[41] R. Oral, P. Bustamante, M. Warnau, A. D'Ambra, M. Guida, G. Pagano, Cytogenetic and developmental toxicity of cerium and lanthanum to sea urchin embryos, Chemosphere 81 (2010) 194-198.